GeoEast-FWI Development and Applications

Zhang Y (BGP), Huang Y (BGP), Chen F (BGP), Wu JL (BGP)

Summary

We present a novel integrated workflow combining Full Waveform Inversion (FWI) and Full Waveform Impedance Inversion (FWII) to achieve high-fidelity seismic model building and imaging. This approach leverages both kinematic (traveltime) and dynamic (amplitude) information to overcome limitations in conventional processing and imaging, particularly in challenging acquisition scenarios. Through global and regional case studies across various geological settings, we demonstrate the efficacy of the FWI+FWII approach in improving velocity and imaging resolution, mitigating migration artifacts caused by multiples and acquisition footprints. It further eliminates free-surface ghosts and source signatures, yielding broadband, high-fidelity reflectivity models for improved geological interpretation. This work highlights the potential of JFWI to elevate seismic imaging, especially in complex geological settings.

Introduction

Full Waveform Inversion has emerged as a powerful technique for inverting high-resolution velocity models, playing a crucial role in revealing complex geological settings. Traditionally, FWI has been employed primarily for velocity model updates to support seismic migration. However, recent developments have expanded its utility beyond model building, demonstrating its capability for high-fidelity seismic imaging through high-frequency velocity inversion (Zhang et al., 2020) or direct reflectivity inversion (Yang et al., 2021).

In this work, we present a Joint Full Waveform Inversion (JFWI) strategy that simultaneously inverts for both the velocity and impedance models within a unified FWI framework. The method begins with Phase-Driven Full Waveform Inversion (PDFWI), which focuses on extracting robust traveltime information to recover the velocity model. This is followed by FWII, which leverages amplitude variations in the data to estimate the band-limited impedance model. Within each iteration, the FWI algorithm extracts near-angle images for impedance inversion and far-angle images for velocity inversion. The resulting broadband impedance model offers a valuable product for geological interpretation or can be transformed into a conventional stacked reflectivity image for structural analysis.

Theory

Given velocity v and impedance $I = \rho v$, where ρ denotes density, we consider the wave equation propagator:

$$L(v, I) = d(\mathbf{x}_r; t; \mathbf{x}_s). \tag{1}$$

Here, d represents the simulated data, with $\mathbf{x}_s$ and $\mathbf{x}_r$ being the source and receiver locations, respectively. Assuming the operator L is isotropic acoustic, its formulation is given by

$$\begin{cases} \left(\frac{1}{v^2(\mathbf{x})} \frac{\partial^2}{\partial t^2} - \frac{I(\mathbf{x})}{v(\mathbf{x})} \nabla \frac{v(\mathbf{x})}{I(\mathbf{x})} \cdot \nabla \right) p(\mathbf{x}; t; \mathbf{x}_s) = \delta(\mathbf{x} - \mathbf{x}_s) f(t), \\ d(\mathbf{x}_r; t; \mathbf{x}_s) = p(\mathbf{x}_r; t; \mathbf{x}_s), \end{cases} \tag{2}$$

where p denotes pressure, and $f(t)$ is the source signature. Our JFWI aims to find the optimal velocity and impedance models to minimize the data misfit between

modelled data *d* and field data *D*, as defined by the objective function:

$$E(v,I) = \min_{v,I} \frac{1}{2} \iiint \left(D - L(v,I)\right)^2 \, dt d\boldsymbol{x}_s d\boldsymbol{x}_r \,. \qquad (3)$$

Based on the true amplitude migration theory, we calculate the gradients of equation (3) by applying velocity perturbation δv and impedance perturbation δI in equation (2), leading to the pseudo-inverse formulation (Zhang et al., 2014):

$$sin^2\theta \frac{\delta v}{v} + cos^2\theta \frac{\delta I}{I} = -32\pi \iiint \frac{v(\boldsymbol{x})}{sin\theta'} cos^2\theta' \, \delta(\theta' - \theta) \frac{p_F(\boldsymbol{x};\omega;\boldsymbol{x}_s) p_B(\boldsymbol{x};\omega;\boldsymbol{x}_s)}{i\omega} d\boldsymbol{x}_s d\theta' d\omega \,, \quad (4)$$

where p_F represents the wavefield simulated through forward propagation, as define by equation (1), while δp_B denotes the wavefield propagated backward from the data residual. θ is the subsurface reflection angle. The delta function $\delta(\theta - \theta')$ enforces angle decomposition of the image. Equation (4) implies that the impedance perturbation $\delta I/I$ can be predicted from near angle images, while the velocity perturbation $\delta v/v$ can be estimated using far-angle images. This differentiation allows us to separate the velocity and impedance effects and invert them simultaneously in every iteration. Notably, our implementation circumvents the need for explicit angle decomposition by embedding angle sensitivity directly into the update kernel, reducing computational cost significantly.

Given the assumption that the velocity is sufficiently accurate and the traveltime information in the simulated data aligns with that of the field data, equation (4) can be used to invert only for impedance by focusing on amplitude matching. This process forms the basis of FWII, which serves as a powerful amplitude-preserving imaging tool. To transform the inverted impedance model $I(x)$ into a conventional reflectivity image suitable for structural interpretation, we use the following directional derivative-based reflectivity approximation:

$$R(\mathbf{x}) = sgn\left(\frac{\partial I}{\partial z}\right) \frac{1}{2I} \sqrt{\left(\frac{\partial I}{\partial x}\right)^2 + \left(\frac{\partial I}{\partial y}\right)^2 + \left(\frac{\partial I}{\partial z}\right)^2} \,. \qquad (5)$$

Equation (5) enhances structural imaging by combining vertical and lateral impedance gradients, producing a reflectivity volume akin to that from zero-angle migration but derived entirely from FWII.

Examples

In the first example, we embedded the SEG logo into the density model, while the velocity model was adopted from a real land acquisition project. We generated a synthetic dataset up to 90hz frequency, with a source spacing of 50m by 50m and receiver spacing of 100m by 100m. As illustrated in Figure 1a, the resulting dataset exhibits significant aliasing in both the common-source and common-receiver domains due to the coarse acquisition geometry. In addition, we simulated a realistic acquisition footprint by removing all sources and receivers located near a predefined surface facility map, introducing non-uniform spatial sampling and illumination gaps.

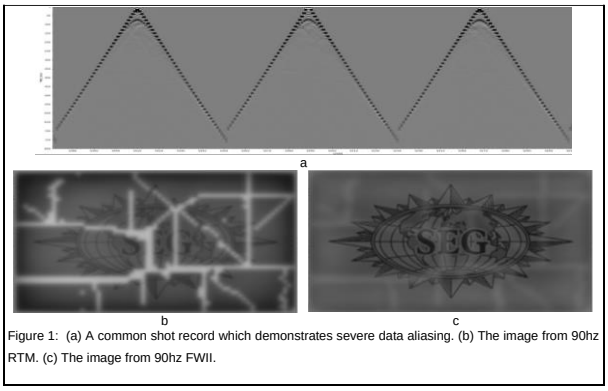

Figure 1: (a) A common shot record which demonstrates severe data aliasing. (b) The image from 90hz RTM. (c) The image from 90hz FWII.

Figures 1b and 1c present a comparison between Reverse Time Migration (RTM) and FWII images derived from the aliased 90hz dataset. The RTM result exhibits prominent high-frequency swing artifacts and imaging discontinuities associated with data aliasing and missing coverage respectively. In contrast, the FWII image demonstrates significant improvements in continuity and resolution. It effectively suppresses high-frequency swings induced by aliasing and compensates for acquisition gaps, thereby producing a more geologically plausible and structurally coherent impedance model.

We next demonstrate the effectiveness of the PDFWI + FWII strategy on a field dataset acquired in the Santos Basin, offshore Brazil. The survey employed an OBN

configuration consisting of 954 nodes arranged in a hexagonal pattern, with a node spacing of 375 m × 325 m. Shots were densely spaced at 50m by 50m, and the survey recorded offsets of up to 20 km, providing long-offset, wide-azimuth coverage suitable for FWI. In the first stage, we applied PDFWI to recover the background velocity model using frequencies up to 20 Hz (Figure 2). The inverted velocity captured both large-scale structures and fine stratigraphic details, benefiting from the wide-angle illumination and robust multiscale inversion scheme. In the second stage, we performed FWII to reconstruct the impedance model using higher frequency components up to 30 Hz (Figure 3a). The resulting impedance volume was subsequently transformed into a broadband reflectivity image using directional derivatives (Figure 3b). Comparing with 30hz RTM image using the legacy velocity model (Figure 3c), we see significant imaging quality and structure improvements, especially in the pre-salt regions, where some imaging interference caused by interbed multiples was much attenuated.

In the third example, we performed TTI JFWI to iteratively invert the velocity and impedance for a shallow water OBN dataset from the East China Sea. The initial model, derived from tomography, captures the general shape and traveltime information but lacks structural detail. By employing 12Hz JFWI, we enhanced the velocity resolution, revealing critical fine details of basement structures and terminations. We further conducted FWII up to 60hz, utilized field-recorded pressure data with minimal preprocessing, including only debubbling and swell noise removal. The direct RTM result showed significant contamination from multiples (Fig. 4a). However, as FWII iteratively updated the impedance, it effectively attenuated artifacts caused by surface and interbed multiples, revealing the true geology (Fig. 4b). This process also removed ghosts and source signatures, resulting in a high-fidelity broadband reflectivity model that greatly enhances the identification and interpretation of shallow channels, fault structures, and intricate geological features.

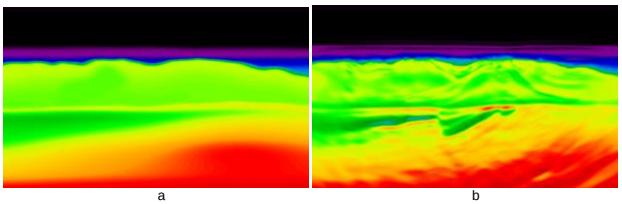

a b

Figure 2: FWI application to a Santos Basin OBN dataset. The initial velocity model (a) and the inverted velocity model using 20hz FWI.

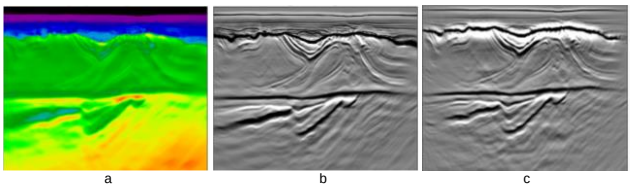

a b c

Figure 3: a: The inverted impedance from 30hz FWII. b: The converted reflectivity image from a. c: 30hz RTM image using the legacy velocity in Figure 2a.

Conclusions

We have developed a novel JFWI approach that simultaneously inverts for both velocity and impedance models, leveraging travel time and amplitude information from seismic data. Through theoretical development and practical examples, our research demonstrates significant improvements in seismic imaging quality. The method enhances velocity resolution and reveals fine structural details, while FWII effectively attenuates artifacts caused by multiples and acquisition footprints. It further eliminates free-surface ghosts and source signatures, yielding broadband, high-fidelity reflectivity models for improved geological interpretation. This work highlights the potential of JFWI to elevate seismic imaging, especially in complex geological settings.

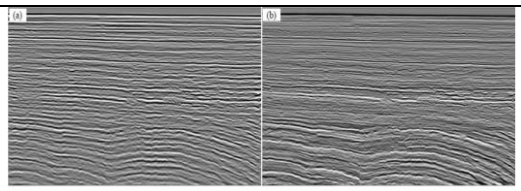

a b

Figure 4: Reflectivity image comparison. (a) An inline RTM image showing contamination by multiples. (b) Reflectivity image converted from FWII using the same input as in (a), demonstrating significant attenuation of multiple interference.

Acknowledgements

We gratefully acknowledge SeisWave Corp. for their collaboration throughout this research and development

work. We also extend our sincere thanks to our colleagues, Yang Yang, Han Yin, Lian Duan, Hui Chen, Tiankui Yin, Zhengzheng Zhou, Wei Wang, Jiawen Song and Kebin Wang, for their valuable contributions to the technical development and seismic data processing work.

References

1. Yang, Y., J. Ramos-Martinez, N. D. Whitmore, G. Huang, and N. Chemingui, 2021, Simultaneous inversion of velocity and reflectivity: 1st International Meeting for Applied Geoscience & Energy, SEG/AAPG, Expanded Abstracts.
2. Zhang Y., Ratcliffe A., Robert G. and Duan L. [2014]. Amplitude-preserving reverse time migration: From reflectivity to velocity and impedance inversion, Geophysics, 79(6), S271-S283.
3. Zhang, Z., Z. Wu, Z. Wei, J. Mei, R. Huang, and P. Wang, 2020, FWI imaging: Full-wavefield imaging through full-waveform inversion: 90th Annual International Meeting, SEG, Expanded Abstracts, 656–660.